ARTICLES
https://doi.org/10.1038/s41560-022-01078-7

nature energy

OPEN

Unveiling microscopic carrier loss mechanisms in 12% efficient $Cu_2ZnSnSe_4$ solar cells

Jianjun Li[1,6] ✉, Jialiang Huang[1,6], Fajun Ma[1,6], Heng Sun[1], Jialin Cong[1], Karen Privat[2], Richard F. Webster[2], Soshan Cheong[2], Yin Yao[2], Robert Lee Chin[1], Xiaojie Yuan[1], Mingrui He[1], Kaiwen Sun[1], Hui Li[3], Yaohua Mai[4], Ziv Hameiri[1], Nicholas J. Ekins-Daukes[1], Richard D. Tilley[2], Thomas Unold[5], Martin A. Green[1] and Xiaojing Hao[1] ✉

Understanding carrier loss mechanisms at microscopic regions is imperative for the development of high-performance polycrystalline inorganic thin-film solar cells. Despite the progress achieved for kesterite, a promising environmentally benign and earth-abundant thin-film photovoltaic material, the microscopic carrier loss mechanisms and their impact on device performance remain largely unknown. Herein, we unveil these mechanisms in state-of-the-art $Cu_2ZnSnSe_4$ (CZTSe) solar cells using a framework that integrates multiple microscopic and macroscopic characterizations with three-dimensional device simulations. The results indicate the CZTSe films have a relatively long intragrain electron lifetime of 10–30 ns and small recombination losses through bandgap and/or electrostatic potential fluctuations. We identify that the effective minority carrier lifetime of CZTSe is dominated by a large grain boundary recombination velocity (~10^4 cm s^{-1}), which is the major limiting factor of present device performance. These findings and the framework can greatly advance the research of kesterite and other emerging photovoltaic materials.

Photovoltaics have been identified as the most attractive renewable energy that can be used to mitigate escalating global climate change[1]. Large-scale deployments of photovoltaic energy require stable, abundant and low-toxic materials similar to silicon (Si) (ref. [2]), which has stimulated the worldwide interest in new inorganic photovoltaic materials such as chalcogenides, oxides, pnictides and halides[3–5]. Kesterite $Cu_2ZnSn(S,Se)_4$ (CZTSSe) has emerged as one of the most compelling candidates due to its stable structure, abundancy, environmental benefits and its large potential for high power conversion efficiency (PCE)[6,7]. Although CZTSSe solar cells have reached the highest PCE (12.6% to 13.0%) among the thermodynamically stable emerging inorganic materials[8–10], their PCE is still far from a commercialization-viable level.

To allow low-cost processing, CZTSSe, like many other emerging inorganic solar cells, often uses polycrystalline thin films as light absorbers and follows the heterojunction architecture[3]. This device architecture accommodates a significant amount of imperfect crystalline structures, mainly grain boundaries and grain surfaces. At these regions, dangling bonds, elastic strain fields and atomic composition segregations may introduce electronic states within the energy bandgap with higher density than that in the grain interiors. These bandgap states may act as carrier traps and/or effective recombination centres depending on their transition energy level and relative capture cross-section for holes and electrons, thus imposing serious limitations to the minority carrier lifetime and carrier mobilities[11]. Consequently, the photovoltaic performance of polycrystalline absorbers is usually inferior to that of crystalline absorbers[12], unless the grain boundaries and grain surfaces are electrically benign, such as the case of hybrid halide perovskite[13], or can be well passivated, such as in the cases of CdTe and $CuInGa(S,Se)_2$ (CIGSSe)[14,15]. Therefore, understanding the carrier loss mechanisms at these microscopic regions is imperative for achieving high-performance CZTSSe and other emerging inorganic thin-film solar cells.

Despite the critical importance of these microscopic carrier loss mechanisms in inorganic materials, the number of investigations regarding these processes is rather limited. For CZTSSe, due to the multiple competitive secondary phases and complex intrinsic defect system[16], most efforts have been directed to the bulk and heterojunction interfaces[17–20]. Although some properties of the grain interiors and grain boundaries, such as intragrain crystallinity defects and band bending at the grain boundaries, have been investigated using high-resolution structural and electrical analysis, respectively[21,22], detailed loss mechanisms in these microscopic regions, especially grain boundary recombination and grain interior carrier lifetime and their impact on the device performance, remain unknown. This, as a critical gap between the understanding of CZTSSe and its mature cousins CdTe and CIGSSe, can be one of the key origins of the efficiency stagnation of CZTSSe in recent years, thus requiring urgent comprehensive investigation.

Herein, we unveil the microscopic carrier loss mechanisms in state-of-the-art efficiency selenide-kesterite $Cu_2ZnSnSe_4$ (CZTSe) solar cells by establishing a framework that integrates multiple micro-structural and macroscopic optoelectronic characterizations with three-dimensional (3D) device simulations, building on a recent approach demonstrated by Krause et al. for CIGSSe solar cells[23]. We show that the grain boundary recombination limits the effective carrier lifetime of bulk kesterite. The associated grain

[1]Australian Centre for Advanced Photovoltaics, School of Photovoltaic and Renewable Energy Engineering, University of New South Wales, Sydney, New South Wales, Australia. [2]Electron Microscope Unit, Mark Wainwright Analytical Centre, University of New South Wales, Sydney, New South Wales, Australia. [3]Beijing National Laboratory for Condensed Matter Physics, Institute of Physics, Chinese Academy of Sciences, Beijing, China. [4]Institute of New Energy Technology, College of Information Science and Technology, Jinan University, Guangzhou, China. [5]Helmholtz-Zentrum für Materialien und Energie, Berlin, Germany. [6]These authors contributed equally:Jianjun Li, Jialiang Huang, Fajun Ma. ✉e-mail: jianjun.li@unsw.edu.au; xj.hao@unsw.edu.au

boundary recombination velocity of kesterite, at a level of 10^4 cm s^{-1}, is one to two orders of magnitude larger than that of CIGSSe and CdTe[23,24]. The intragrain minority carrier lifetime is estimated to be 10–30 ns, while the net carrier density is around 1.8×10^{15} cm^{-3}. It seems that the well-recognized open-circuit voltage (V_{OC}) losses due to bandgap fluctuation and/or electrostatic potential fluctuation are small. Instead, the dominating loss mechanisms of current state-of-the-art CZTSe solar cells are associated with the severe non-radiative recombination at grain boundaries. Further efficiency improvement towards 20% requires substantial grain boundary passivation and increase of net carrier density.

Photovoltaic performance and device structure

We used CZTSe absorbers fabricated by the same method used for our reported 12.5% record CZTSe cells[25]. Details of the fabrication processes can be found in the Methods section. The solar cells fabricated on these absorbers achieve PCEs between 11.0% and 12.5% and an average PCE of 11.8% (Supplementary Fig. 1), representing state-of-the-art performance. Figure 1a,b shows the current density–voltage (J–V) and external quantum efficiency (EQE) of one of the best devices used for characterizations in this study. The total area (0.24 cm^2) efficiency is 12.45 %, with a V_{OC} of 479 mV, a fill factor (FF) of 70.45% and a short-circuit current density (J_{SC}) of 36.9 mA cm^{-2} (integrated J_{SC} from EQE is 37.0 mA cm^{-2}). The diode ideality factor (A) extracted from corresponding dark J–V data is 1.4 and the diode reverse saturation current (J_0) is 8.1×10^{-8} A cm^{-2} (Supplementary Fig. 2). The J_{SC} is much lower than the previous 11.6% efficiency record CZTSe device from IBM (40.6 mA cm^{-2}) (ref. [26]), which could be attributed to the relatively low transmittance of the window layer at the long-wavelength region, as discussed in our previous work[25] and the recombination in the microscopic regions as will be discussed in the following sections.

On the top, the CZTSe absorber shows large and compact grains (>1 µm), while at the bottom, the grains are smaller and voids can be seen (Fig. 1c). The secondary ion mass spectroscopy (SIMS) depth profile (Fig. 1d) indicates the CZTSe absorber has a high Zn concentration at the surface and high Sn concentration at the bottom. Segregations of Zn (probably ZnSe) could be observed at both the top and the bottom of the CZTSe film in the scanning transmission electron microscopy coupled with energy-dispersive X-ray spectroscopy (STEM-EDS) mapping (Fig. 1e). Many Sn-rich and Cu-rich small grains (probably $SnSe_x$, $Cu_{2-x}Se$ or Cu_2SnSe_3) can be noticed at the bottom region near the $MoSe_2$ layer, in agreement with the SIMS profile. The signal of Cd is fully confined between CZTSe and ZnO, showing no significant diffusion into the CZTSe absorber or grain boundaries.

Carrier transport at front and rear interfaces

Results of surface Raman mapping on a 40×40 µm^2 bare CZTSe absorber indicate that most of the front surface is covered with a ZnSe layer (Fig. 2a–c). This ZnSe layer is in situ grown, which could be correlated to the excessive Zn of the Zn-rich and Cu-poor local chemical environment in the surface region during the synthesis of CZTSe[25]. Further high-resolution STEM (HR-STEM; Fig. 2d) shows the presence of a locally epitaxially grown 8–12 nm thick ZnSe nanolayer (also observed by EDS line scan, Supplementary Fig. 3) along with the (200) orientation. With the almost identical (200) interplanar spacing between CZTSe and ZnSe (0.283 nm, Fig. 2d), no dislocation is observed at the CZTSe/ZnSe interface, showing a near-perfect heterointerface with largely suppressed interfacial lattice defects. In comparison, the CZTSe absorber without ZnSe nanolayer shows a high density of dislocations at the CZTSe/CdS heterointerface (Supplementary Fig. 4). Additionally, ZnSe has a wide bandgap of 2.7 eV with a conduction band minimum 0.86 eV higher and a valence band maximum 0.78 eV lower than that of CZTSe[27]. These large electron and hole barriers could repel electrons and holes, respectively, preventing them from recombining at the heterojunction interface, thus effectively suppressing interfacial recombination. On the other hand, due to the large 'spike-like' conduction band offset (0.86 eV) at the ZnSe/CZTSe interface, transport of the photogenerated electrons across this interface may rely on the tunnelling and/or thermionic emission processes depending on the device temperature. It is noted that a continuous ZnSe layer with 8–12 nm thickness may be too thick for tunnelling, which may block the electron current[28]. In another HR-STEM image (Supplementary Fig. 5), the thickness of ZnSe varies in a region of 4.7–12 nm. The thin ZnSe-layer (<5 nm) regions may provide the main electron transport channels across the CZTSe/ZnSe/CdS interface if tunnelling is dominating. On the other hand, according to Mendis' model[29], at room temperature, the large spike-like conduction band offset at the ZnSe/CZTSe interface can be greatly suppressed because the ZnSe nanolayer can be easily fully depleted, enabling thermionic emission of the photocurrent across the junction interface.

Figure 2e shows the temperature-dependent diode ideality factor, A, extracted from the dark J–V curves (Supplementary Fig. 7). A is larger than 2 when the temperature is lower than 200 K, suggesting that the device does not behave as an ideal diode in this temperature region[30] and that the tunnelling process at the CZTSe/ZnSe interface dominates the current transport in this temperature region[31]. Contrastingly, A is around 1.5 without significant change when the temperature is in the range of 260–320 K, indicating the dominating current transport mechanism is likely to be thermionic emission in this temperature region, where it is possible to extract the recombination activation energy, E_A, using the one-diode model[32]:

$$V_{OC} = \frac{E_A}{q} - \frac{Ak_BT}{q}\ln\left(\frac{J_{00}}{J_L}\right), \qquad (1)$$

where q is the unit charge, k_B is the Boltzmann's constant, T is the temperature, J_{00} is the prefactor of diode current and J_L is the photocurrent. Here J_{00}, J_L and E_A are assumed to be weakly temperature-dependent in the temperature region used for fitting[32]. The temperature-dependent V_{OC} shows good linear behaviour in this temperature region (Fig. 2f), and the fitted E_A is 1.025 ± 0.005 eV, well-aligned to the bandgap of the CZTSe absorber ($E_g=1.02$ eV, as shown in Fig. 3e). This indicates that the E_A deficit compared with E_g is no longer a limitation in these CZTSe devices, owing to the passivated heterojunction interface by the epitaxial ZnSe nanolayer and the suppressed bandgap/potential fluctuation as reported previously[25].

The blocking barrier height of the back contact interface is derived from the temperature-dependent series resistance (R_S) over the 200 K to ~320 K temperature range where the device behaves consistently with the thermal emission model[33]. The fitted barrier height is only 11 ± 5 meV (Fig. 2g), much smaller than the previously reported value[34], indicating a quasi-ohmic contact at the back contact interface. The result of cross-sectional Kelvin probe force microscope (KPFM) measurements also confirms that the fine grain layer and the $MoSe_2$ layer do not introduce a hole-transporting barrier at the back contact interface (Supplementary Figs. 8 and 9).

Potential fluctuations

We investigated the lateral electrostatic potential fluctuation between grains and the band bending at grain boundaries by means of combining atomic force microscopy (AFM) and Kelvin probe force microscopy (KPFM) on a fresh cleaved cross-section, as shown in Fig. 3a,b. The horizontal line scan of contact potential difference (CPD) (Fig. 3c) indicates a relatively uniform electrostatic potential distribution between the grains even though the topology fluctuation is large, highlighting that the impact of the topology on the CPD is small. The electrostatic potential fluctuation is only 5.4 meV,

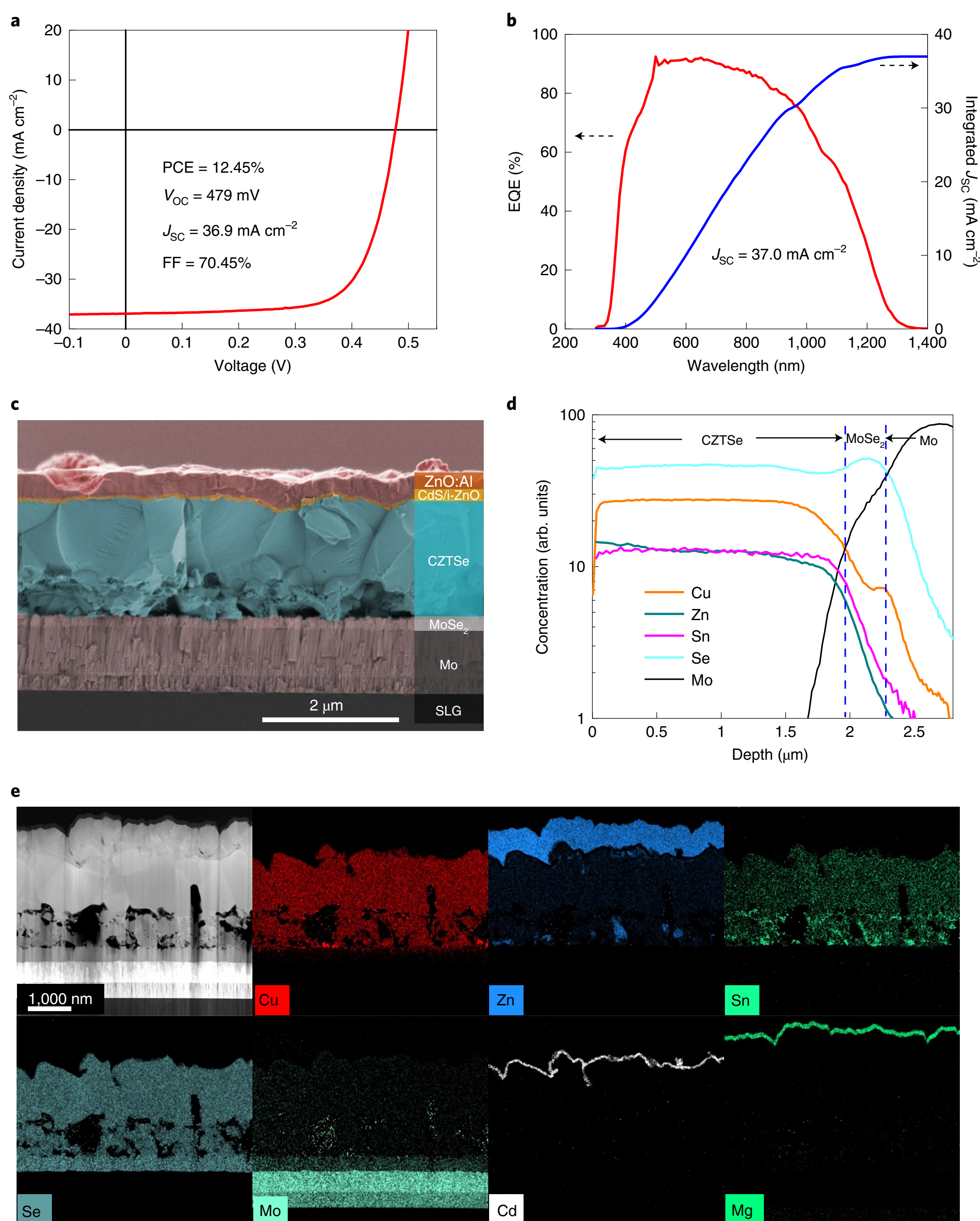

Fig. 1 | Device performance, morphology and element distribution. a,b, *J*–*V* (**a**) and EQE (**b**) measurements of one of the best CZTSe cells with total area (0.24 cm^2) efficiency of 12.45% with anti-reflection coating. **c**, Cross-sectional SEM image of a CZTSe device. The device structure from bottom to top is soda lime glass (SLG)/Mo/$MoSe_2$/CZTSe/CdS/i-ZnO/ZnO:Al. **d**, Element SIMS depth profile of the CZTSe absorber. **e**, The cross-sectional TEM image and the corresponding EDS element mapping of Cu, Zn, Sn, Se, Mo, Cd and Mg. The cross-sectional STEM sample was prepared with a focused ion beam.

which is negligible compared with the resolution of CPD (~10 mV). The band bending at GB1 is 8 meV (Fig. 3d), which is also negligible, the same as the band bending of GB2 to GB5 (Supplementary Fig. 10). The local chemical composition near grain boundaries was investigated using an EDS line scan. A small Cu peak is observed at the grain boundary region (Supplementary Fig. 11), which has also been observed in other CZTSe and CIGS solar cells[35,36], and has been deemed detrimental for device performance.

The potential fluctuation is further investigated by analysis of the internal quantum efficiency (IQE, Supplementary Fig. 12) and photoluminescence (PL) spectra. The PL emission energy, E_{PL} (1.01 eV), is only slightly lower than the bandgap (1.02 eV) determined from the inflection of the IQE curve (peak of −dIQE / dλ, Fig. 3e). The PL peak is quite broad, though no obvious red shift is observed. This PL peak broadening can be attributed to band tailing states arising from bandgap and/or electrostatic potential fluctuation, both of which can be estimated using the absorption edge derived from the tail of the IQE curve (Supplementary Discussion 1) (ref. [37]). Bandgap fluctuations can be described by a Gaussian distribution of local absorption coefficient with a standard

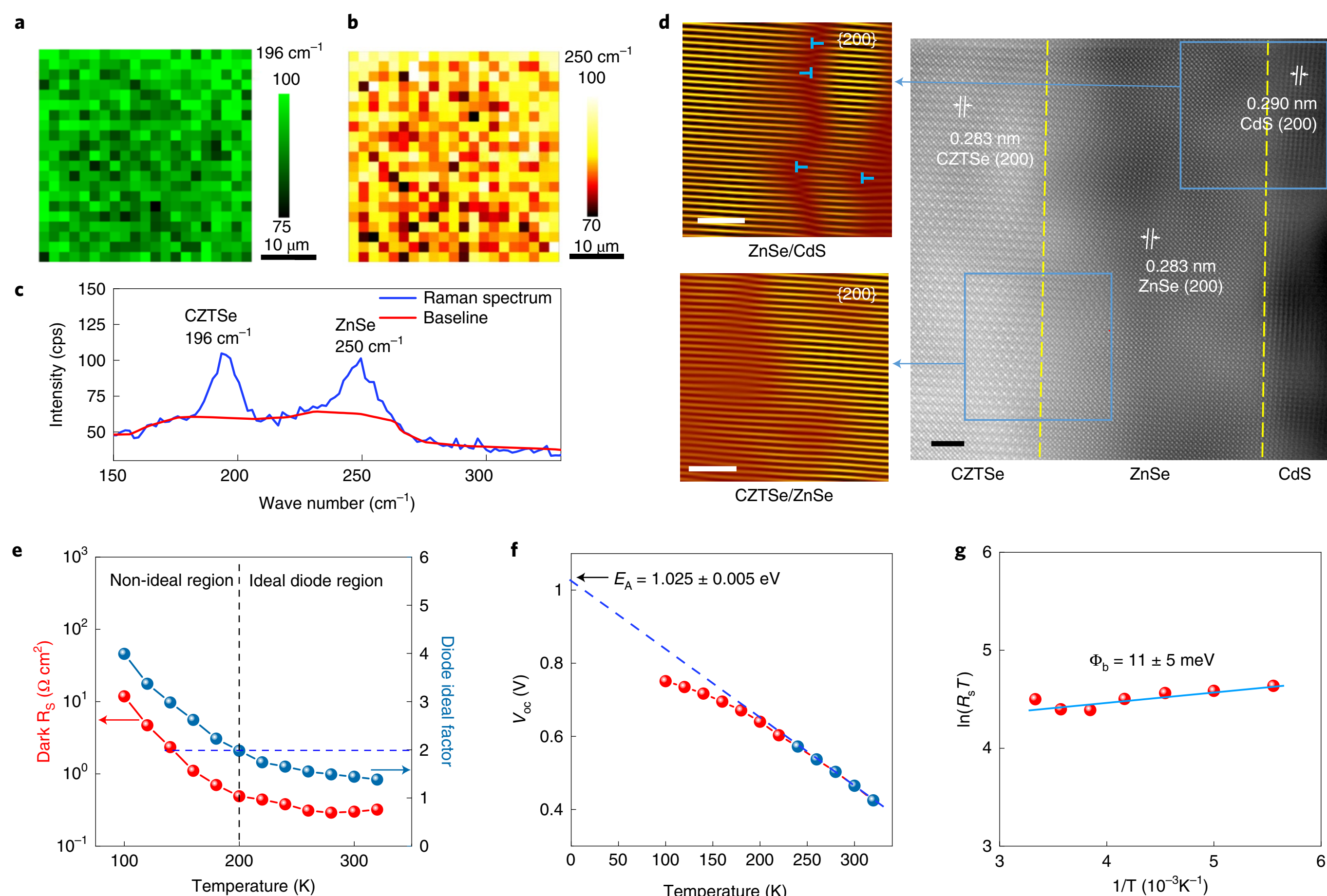

Fig. 2 | Structure and carrier transport performance of the front and rear interfaces. a,**b**, Colour-coded Raman intensity mapping at peak positions of 196 cm^{-1} (A mode of CZTSe) (**a**) and 250 cm^{-1} (A1 mode of ZnSe) (**b**), respectively (without baseline subtraction). The Raman mapping was performed using a 441 nm He-Cd laser as excitation. **c**, Average Raman spectrum of the mapping and the corresponding baseline. The unit cps. means count per second. The baseline-subtracted Raman spectrum is shown in Supplementary Fig. 6. **d**, HR-STEM image and the colour-coded inverse fast Fourier transformation images of the selected reflections revealing the dislocations (T marked) at the CZTSe/ZnSe/CdS heterointerface. The interplanar spacings are indicated in the HR-STEM figure. The yellow dashed lines roughly indicate the boundaries of different phases. The length of all the three scale bars is 2 nm. **e**, Temperature-dependent series resistance (Rs) and diode ideality factor extracted from temperature-dependent *J–V* curves (Supplementary Fig. 7). For each metric, the line on top of data is a guide to the eye. The black dashed line indicates the boundary between the ideal device region and non-ideal device region. The horizontal dashed blue line indicates where the diode ideality factor is 2. **f**, Plot of V_{OC} versus temperature and the linear fit (dashed blue line) of the recombination activation energy E_A. The data points coded with blue are selected for the linear fitting. The red line on top of data is a guide to the eye. **g**, Plot of ln (R_ST) versus 1/T and the linear fitting showing back contact barrier height. R_s is the series resistance and T is the temperature.

deviation of σ_g (ref. [37]). The fitted σ_g is 48 meV (Supplementary Fig. 13), which is significantly lower than some previous analysis[37] but in good agreement with more recent findings[38]. Because the local bandgap fluctuation observed in cathodoluminescence (CL) mapping is within 5 meV, these fluctuations would have to occur on length scales smaller than the spatial resolution of CL measurement (several 100 nm). Alternatively, average electrostatic fluctuations, γ_{opt}, can be estimated from the Shklovskii and Efros model[39], yielding a value of 20 meV (Fig. 3f), which also agrees with the estimated Urbach tail energy (E_u). The loss of radiative limit V_{OC} ($V_{OC,rad,loss}$) due to the lateral potential fluctuation can be estimated to be 44 mV or 7.7 mV due to either σ_g or γ_{opt}, respectively, by the following equation[40]:

$$V_{oc,rad,loss} = \gamma^2/2qk_BT \quad (2)$$

where γ is either σ_g or γ_{opt}. Nevertheless, the V_{OC} loss due to these fluctuations in our cells is rather small compared with the non-radiative loss mechanisms that will be discussed in the following sections.

Carrier collection and free carrier density

We performed electron beam-induced current (EBIC) measurement to investigate the carrier collection in the CZTSe solar cell. Figure 4a,b shows the SEM and EBIC images of the corresponding cross-section of the CZTSe solar cell at a beam energy of 5 keV. Figure 4c shows a representative cross-sectional line scan extracted from a reasonably flat region without near-horizontal grain boundary and the fitting using the analytical approach described by Nichterwitz et al.[41]. The fitted electron diffusion length is around 250 nm. As the excitation depth of the acceleration voltage used in EBIC (at 5 kV) is estimated to be only about 100 nm (Supplementary Fig. 14), it can be expected that the decay of EBIC in the quasi-neutral region (QNR) may be significantly enhanced by recombination at the unpassivated cross-section surface, thus underestimating the electron diffusion length. For a given fitted electron diffusion length, the upper limit of the intragrain electron diffusion length is estimated to be 1.0 µm using the upper limit of surface recombination velocity (10^7 cm s^{-1}), according to the method described by Nichterwitz et al.[41]. However, we note that this approach is not

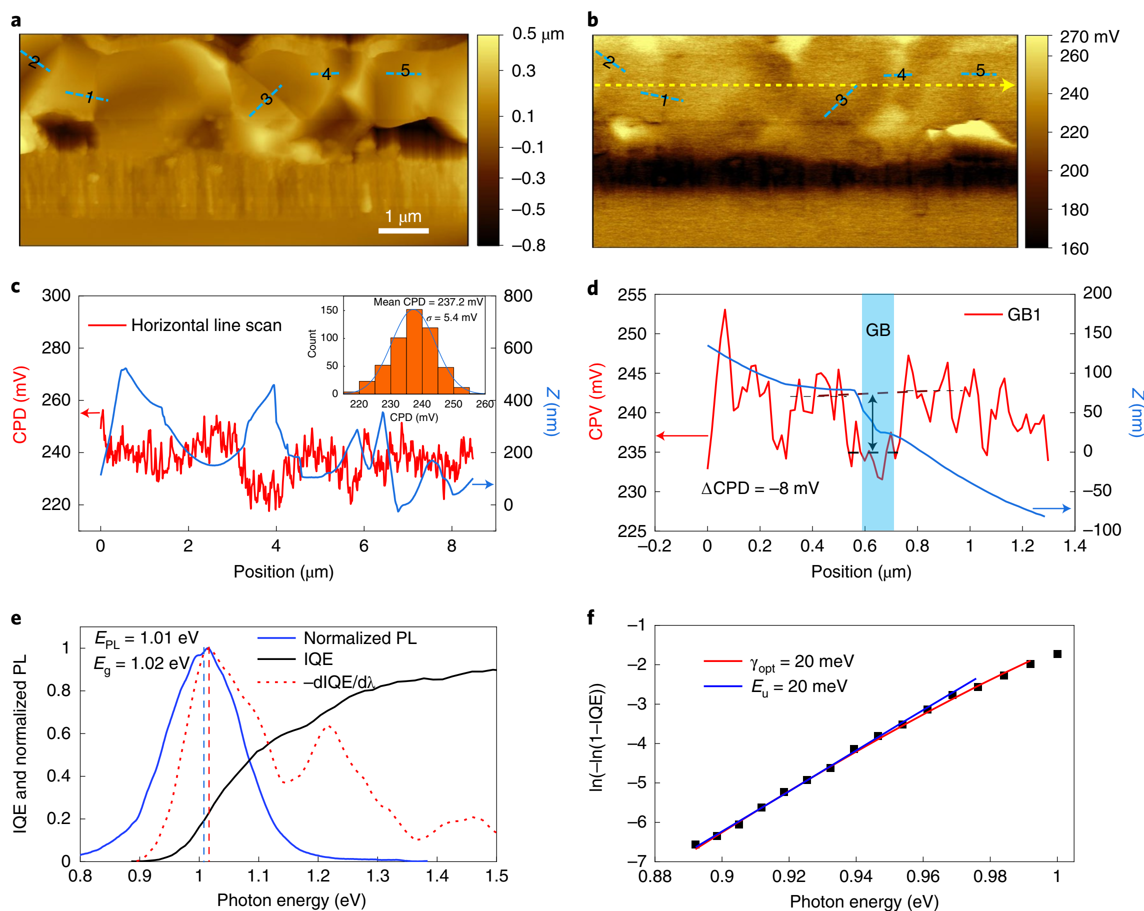

Fig. 3 | Kelvin probe force microscope and electrostatic potential fluctuation. a,b, Topology image measured with AFM (**a**) and the corresponding KPFM image (**b**) of a fresh cleaved CZTSe cell. The blue dashed lines labelled with numbers indicate where the grain boundary profiles were extracted. The yellow (horizontal) dashed line in **b** indicates where the line scan was performed. **c**, Contact potential difference (CPD) and topology profiles (Z) extracted along the yellow (horizontal) dashed line in **b**. Here CPD = $(\Phi_P - \Phi_S)/q$, where Φ_P and Φ_S are the work function of the probe and the measured sample, respectively, meaning CPD increases linearly with the decrease of work function of the measured sample. The inset shows the statistical CPD distribution and the Gaussian fit of the horizontal CPD scan, showing a mean CPD of 237.2 mV and a standard deviation of 5.4 mV. **d**, The CPD and topology profiles of grain boundary (GB) 1 (indicated in **a** and **b**). The blue shade is a guide to the eye showing where the grain boundary is located. Each dashed black line is a guide to the eye roughly indicating the mean CPD around the grain boundary, which is used to define the ΔCPD. The band bending at GB1 is about −8 meV (upward). The CPD and topology profiles of GB2–GB5 are shown in Supplementary Fig. 10. **e**, IQE spectrum (black line), first derivative of IQE (red dashed line) and normalized PL spectrum (blue line) of the high efficiency CZTSe cell. The vertical dashed blue and red lines indicate the PL peak position and the peak position of −dIQE / dλ, respectively. λ is the wavelength. **f**, Plot and fitting of electrostatic potential fluctuation, γ_{opt} (red) using the Shklovskii and Efros model below the bandgap energy and the fitting of the Urbach tail energy, E_u (blue). Detailed fitting models are described in Supplementary Discussion 1.

very accurate given that the cross-section surface is not very flat. The intragrain diffusion length will be further estimated using 3D device simulation.

Considering the large surface roughness of the CZTSe absorber (inset of Fig. 4d), the effective junction interface area can be significantly larger than the device area. On the basis of the AFM measurement (Supplementary Fig. 15), the effective junction interface area is about 1.3 times of the device area. Using the single-side abruption junction mode (ignoring the depletion region in the n-type buffer and window layer), the doping density (N_{DL}) of the CZTSe absorber can be calculated as following[42]:

$$N_{DL} = -C_0^3/2q\varepsilon_0\varepsilon_r A_j^2 C_1, \quad (3)$$

where A_j is the junction interface area and C_0 and C_1 are the static capacitance and the first-order differential capacitance, respectively. With the estimated junction interface area, N_{DL} is calibrated from 3.1×10^{15} cm^{-3} to 1.8×10^{15} cm^{-3} (Fig. 4d). The N_{DL} is the number of bulk acceptor defects that can contribute to the free carrier density. According to the defect activation energy measured using admittance from a similar sample (130 meV) (ref. [25]), the electrical neutral condition and the Fermi–Dirac distribution, these defects are fully ionized (detailed analysis in Supplementary Discussion 2). We thus get an average free carrier density of 1.8×10^{15} cm^{-3}.

In addition, the high spatial resolution of the EBIC image enables us to further investigate the electron transport across the grain boundaries. It is noteworthy that the CZTSe grains underneath near-horizontal grain boundaries, not directly connected to the buffer layer (Supplementary Fig. 16), do not contribute to the EBIC signal. This indicates significant recombination and/or a carrier transport barrier may exist near these grain boundaries or inside these grains, which may be responsible for the additional J_{SC} loss in the long-wavelength region.

Carrier recombination at grain boundaries and grain interiors

The non-radiative recombination velocity at grain boundaries and grain interiors is first qualitatively compared by performing cathodoluminescence (CL) mapping on a directly cleaved cross-section

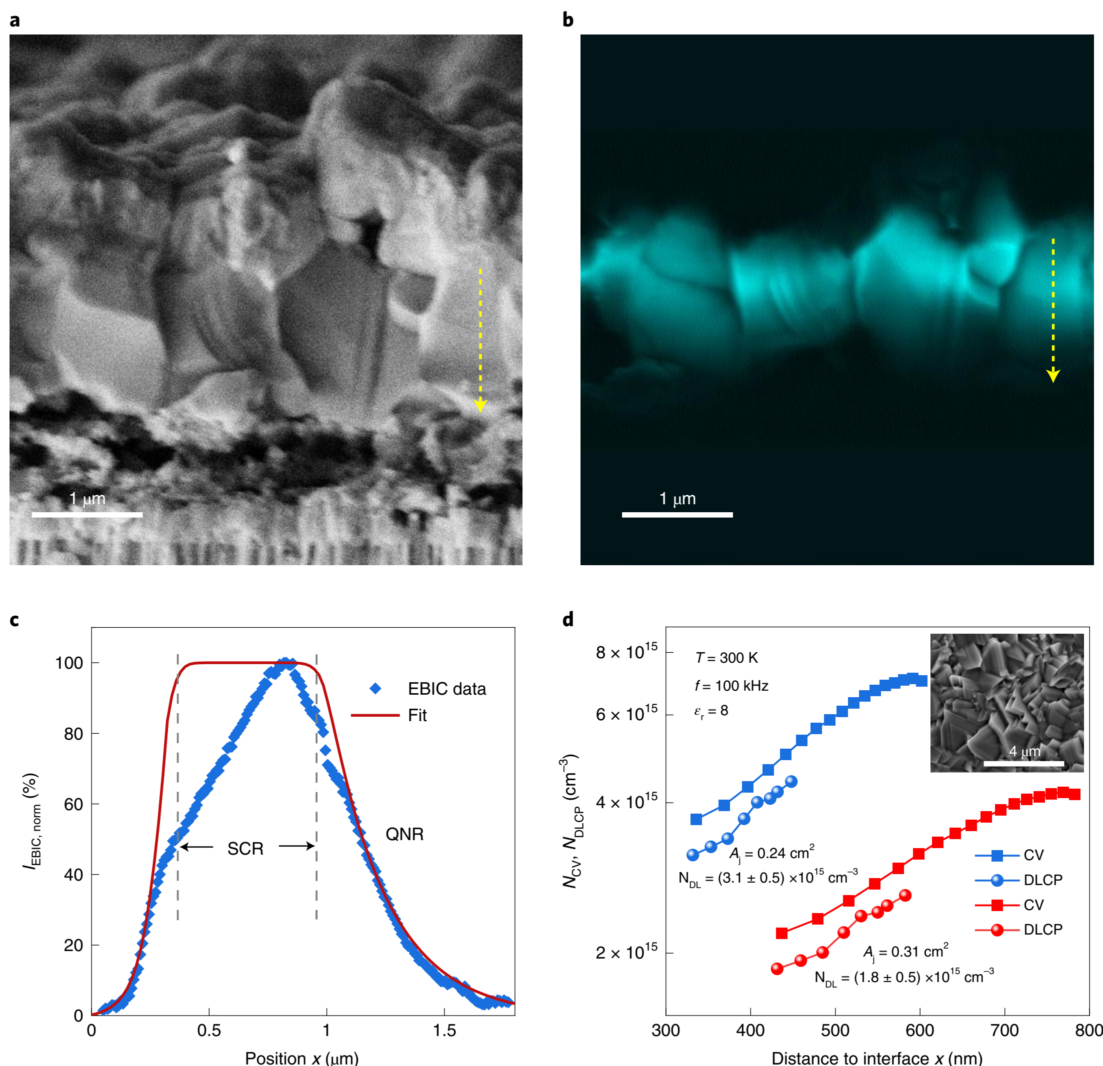

Fig. 4 | Electron beam-induced current and carrier density analysis. a,**b**, Cross-sectional SEM image (**a**) and EBIC image (**b**) of a cleaved CZTSe device. The beam energy was 5 keV. **c**, Normalized EBIC Intensity ($I_{EBIC,norm}$) profile (blue dots) along the dashed yellow arrows shown in **a** and **b** and the fitting with analytical model (red line). The space charge region (SCR) and QNR are separated with the vertical dashed lines. The fluctuation of the EBIC signal is induced by the rough morphology. The regions with protrusions show weak EBIC because of the higher reflection of electron beam, and vice versa. The EBIC signal at the SCR region is severely altered by the non-flat morphology, which may lead to a large error in fitting of depletion region width. The QNR region shows a relatively flat morphology and thus is used for fitting diffusion length in this region. **d**, Carrier density profiles measured with capacity voltage (CV) and drive-level capacity profile (DLCP) with junction area before (blue) and after (red) modification. N_{CV} and N_{DLCP} are apparent carrier densities measured by CV and DLCP, respectively. f is the modulation frequency used for the CV and DLCP measurements. ε_r is the relative dielectric constant of CZTSe. A_j is the junction area. The inset shows the plain view SEM image of a CZTSe absorber.

sample. In the measured region, all the grain boundaries show pronouncedly lower CL intensity compared with the grain interiors (Supplementary Fig. 17), which indicates grain boundaries have much larger non-radiative recombination velocity compared with the grain interiors. To exclude the effect of morphology and quantify the non-radiative recombination velocity at the grain boundaries, S_{GB}, we further performed CL mapping of a focused ion beam (FIB)-prepared cross-section sample. As shown in Fig. 5a, the grains at the top and bottom of the CZTSe layer show comparable CL intensities while the CL intensities at the grain boundaries are much lower compared with the grain interiors. This verifies that the poor carrier collection efficiency in the bottom grains observed in EBIC can be attributed to their relatively larger S_{GB} rather than to the recombination inside the grain interiors. Figure 5b shows CL line scans across two representative grain boundaries. No obvious CL peak energy variation is observed at the grain boundaries (Fig. 5c), indicating the bandgap does not change at the grain boundaries. The value of S_{GB} can be estimated using the decay of CL intensities between grain boundaries and grain interiors, according to the model described by Mendis et al.[43]:

$$\ln\left[\Delta I\left(x\right)\right] = \ln\left[S/(S+1)\right] - x/L, \quad (4)$$

where $\Delta I(x)$ is the relative CL intensity between the grain boundaries and grain interiors, L is the apparent electron diffusion length, S the reduced recombination velocity ($S = S_{GB}\ \tau_{GI}/L$, where τ_{GI} is the minority carrier lifetime of grain interior) and x is the position of the electron beam. The linear fittings of S and L are shown in Fig. 5d. Here we adopt the value of τ_{GI} of 10–30 ns based on the 3D device simulations as will be shown below.

The values of S_{GB} extracted from six grain boundaries (marked in Fig. 5a) are in a range of $(0.15–3.8) \times 10^4$ cm s^{-1}, one to two orders

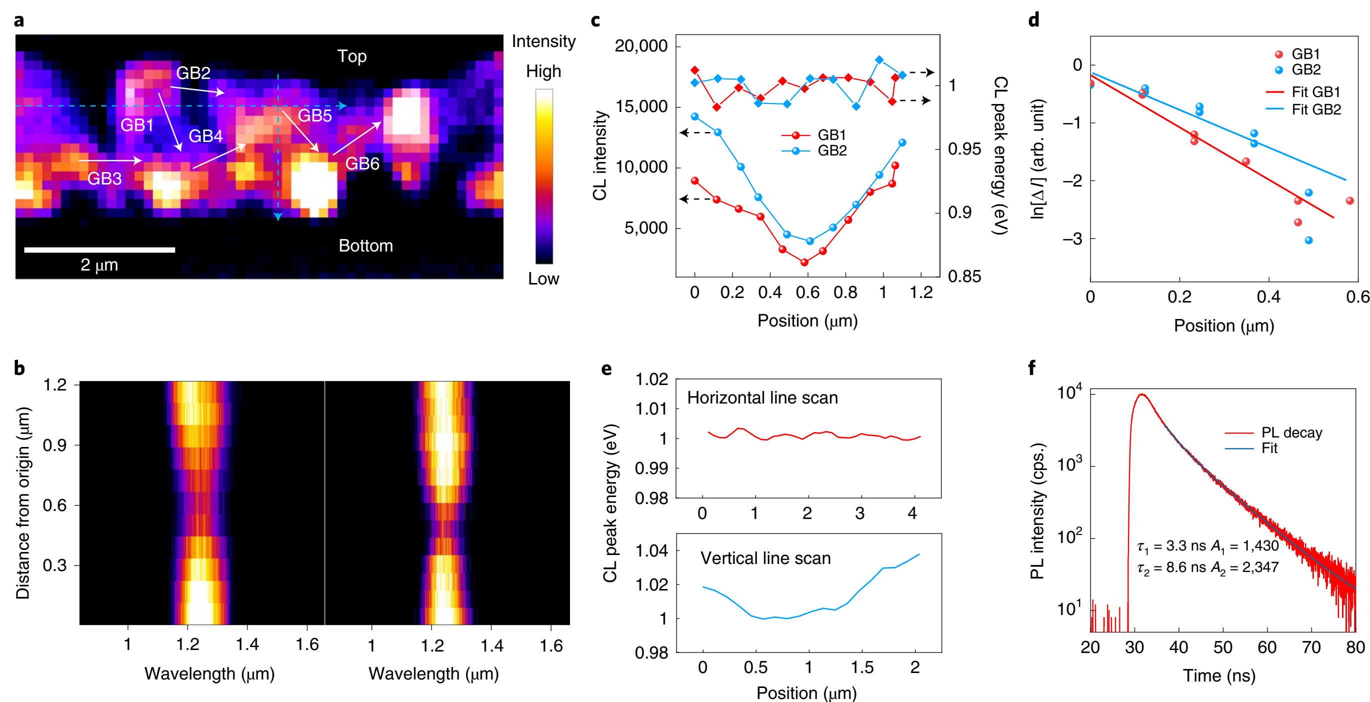

Fig. 5 | CL and PL analysis. **a**, Hyperspectral and intensity-combined CL map acquired at 10 keV from an FIB-prepared cross-sectional sample of CZTSe absorber. The SEM image is shown in Supplementary Fig. 18. The white arrows labelled with grain boundary numbers are where CL profiles are extracted for further analysis.The horizontal and vertical blue dash arrows indicate where line scans are taken. **b**, Spectro-, spatial- and intensity-resolved CL maps of the two representative grain boundaries indicated in **a**. **c**, Extracted CL intensity and peak energy profiles across the two grain boundaries. **d**, ln[Δ*I*] plots of the CL intensity profiles of GB1 and GB2 for positive distance values. The red and blue solid lines are linear regressions. The ln[Δ*I*] plots of GB3–6 are shown in Supplementary Fig. 19. **e**, Extracted CL peak energy profiles along the horizontal and vertical blue dashed arrows indicated in **a**. **f**, TRPL measured with a 532 nm laser and its corresponding double exponential decay fit. The unit cps. means count per second.

of magnitude larger than the value reported for high efficiency CIGSSe and CdTe solar cells[23,24]. As the band bending at grain boundaries is negligible, the effective grain boundary recombination velocity is not affected by band bending and should be close to the S_{GB}. It is noteworthy that the high recombination velocity at the grain boundaries may also exist in sulfur-mixed CZTSSe and CZTS materials, indicating that more pertinent research efforts, such as grain boundary chemistry and passivation strategies are urgently needed for kesterite solar cells.

In addition, we further investigated the bandgap fluctuation in the CZTSe absorber by horizontal and vertical line scans of CL peak energies. The positions of these line scans are indicated in Fig. 5a, and the results are shown in Fig. 5e. The horizontal CL emission peak fluctuation at the region near the junction interface is rather small (<5 meV). In contrast, the front and rear surface regions show slightly increased CL peak energy compared with the bulk by 20–40 meV, which could be attributed to an increased bandgap correlating with the relatively high sodium concentration at the top and bottom (Supplementary Fig. 20). The incorporation of Na is known to slightly increase the bandgap of kesterite[44]. The minimum CL peak energy at the bulk is 1.00 eV (Supplementary Fig. 21), 0.01 eV and 0.02 eV lower than the PL peak energy and bandgap energy, respectively.

To evaluate how the large S_{GB} impacts the optoelectronic quality of CZTSe absorber, we quantitatively correlated the effective minority carrier lifetime to the S_{GB} and the grain size d (Supplementary Discussion 3):

$$\tau_{\mathrm{eff}} \cong \tau_{\mathrm{GB}} \cong \frac{d}{(6-n)\cdot S_{\mathrm{GB}}}, \quad (5)$$

where n is the number of passivated faces of cubic-like grains. Equation (5) suggests that grain size d could also be a critical factor that determines τ_{eff}. Using the value of S_{GB} extracted from CL mapping, the calculated value of τ_{GB} of our CZTSe absorber with a grain size of 1.1 μm is 0.6–4.7 ns, with an average value of 2.5 ns, comparable to the fast decay time measured from time-resolved PL (TRPL) (3.3 ns, Fig. 5f), which is believed to be a key parameter determining V_{OC}[45,46]. Using equation (5), the statistical average S_{GB} in the cells is estimated to be 6.7×10^{3} cm s^{-1} for the CZTSe absorbers with effective minority carrier lifetime of 3.3 ns (measured from TRPL) and grain size of 1.1 μm.

3D device simulations

To further investigate the critical intragrain material parameters (carrier lifetimes and mobilities) and how the microscopic carrier recombination mechanisms impact the device performance, we link the above characterizations into 3D device simulations. The simulations were based on a 3D unit cell established using the equivalent topology extracted from the morphology in the SEM and STEM images (Supplementary Figs. 22–24). The experimentally obtained photo-electronic parameters, including free carrier density, potential fluctuation, bandgap grading and the statistical average S_{GB}, are integrated into the simulation model as fixed parameters (details in Methods and Supplementary Table 1).

Under a reasonable precondition that the minority carrier electrons should have a longer lifetime and mobility than holes, we can get a set of values of intragrain electron and hole lifetimes and mobilities by matching the experimental J–V and EQE data of the 12.45% efficient CZTSe cell. Meanwhile, the radiative loss due to potential fluctuations is simulated and shown to be rather small (Supplementary Fig. 25). Starting from this point, we can first estimate

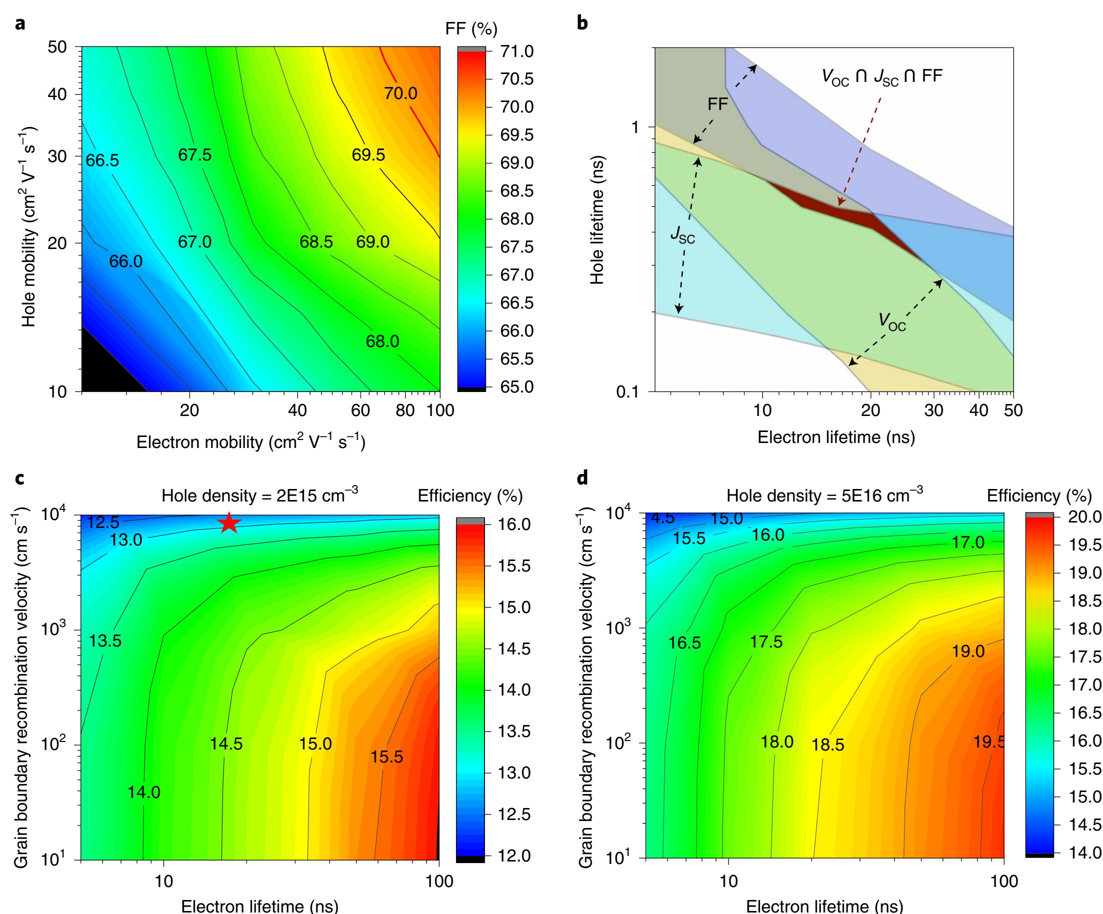

Fig. 6 | 3D device simulations for CZTSe solar cells. a, The simulated contour of FF versus electron and hole mobilities under fixed electron and hole lifetime of 15 ns and 0.3 ns, respectively, which are obtained from fitting *J*–*V* and EQE curves. The simulated J_{SC} and V_{OC} under the same conditions are shown in Supplementary Fig. 26. **b**, Simulated V_{OC} (light yellow), FF (light purple) and J_{SC} (light blue) versus electron and hole lifetimes within ±1% deviation compared with the experimental baseline. The full contours are shown in Supplementary Fig. 27. The overlapped region coloured in dark brown indicates where the electron and hole lifetime can well fit experimental V_{OC}, FF and J_{SC} simultaneously. The other overlapped regions indicate where V_{OC} and J_{SC} (green), J_{SC} and FF (dark blue) and V_{OC} and FF (military green) are well fitted. **c**,**d**, Simulated contours of efficiency against carrier lifetime and grain boundary recombination velocity under hole density of 2×10^{15} cm^{-3} (**c**) and 5×10^{16} cm^{-3} (**d**), respectively. The red star in **c** indicates the current state-of-the-art CZTSe cells. The optical loss is reduced in **d** to an extent that maximum J_{SC} can achieve 40 mA cm^{-2}. The efficiency contours under hole density of between 5×10^{15} cm^{-3} and 2×10^{16} cm^{-3} are shown in Supplementary Fig. 28.

the region of intragrain carrier mobilities by fitting the value of FF and J_{SC} because FF and J_{SC} are sensitive to carrier mobilities while V_{OC} is not. As shown in Fig. 6a, to match the value of FF (70~70.5%), the mobilities of electron and hole have to be in a range of 80–100 cm^2 V^{-1} s^{-1} and 30–50 cm^2 V^{-1} s^{-1}, respectively, which fall within the same regions as that determined by fitting the J_{SC} (Supplementary Fig. 26). The fitted electron mobility is comparable to that measured using time-resolved terahertz spectroscopy (128 cm^2 V^{-1} s^{-1}) (ref. [47]), while the hole mobility is several times higher than that measured from time-resolved terahertz spectroscopy. Then we can estimate the value of electron and hole lifetimes under fixed electron and hole mobility (Supplementary Fig. 27). Figure 6b shows the overlapped region (dark brown) where experimental V_{OC}, FF and J_{SC} can be all well fitted within 1% deviation. The estimated intragrain electron and hole lifetimes are 10–30 ns and 0.3–0.7 ns, respectively. This shows that the intragrain minority carrier lifetime is significantly higher than the effective carrier lifetime. The electron diffusion length thus is estimated to be 1.4–2.8 μm, comparable with the value measured using bias dependent IQE[26].

To identify the efficiency limiting factors and associated step-change directions for further efficiency improvement, we simulated how the efficiency changes with intragrain electron lifetime, grain boundary recombination velocity and hole density. As shown in Fig. 6c,d, if the grain boundary recombination remains at 10^4 cm s^{-1}, the efficiency can hardly be improved by increasing carrier lifetime or carrier density, suggesting that the large grain boundary recombination velocity is the current limiting factor. Additionally, if the carrier density can be improved to 5×10^{16} cm^{-3}, a typical carrier density level for >20% efficient CIGS and CdTe solar cells[23,48], the efficiency can be more easily improved, and ~20% efficiency can be achieved by reducing grain boundary recombination velocity to <10^2 cm s^{-1} and increasing electron lifetime to 100 ns. On the other hand, larger grain size will also lead to better performance (Supplementary Table 2) because both τ_{GB} and τ_{eff} linearly increase with grain size as described by equation (5).

Discussion

The above results indicate the device performance of the investigated 12.45% efficient CZTSe solar cells is mainly limited by the large grain boundary recombination velocity and the relatively low net carrier density. There are reported strategies to increase the net carrier density without introducing secondary phases, such as indium and lithium doping[49,50]. However, investigation of grain boundary passivation for kesterite materials is rather limited.

The grain interior carrier lifetime is in a range of 10–30 ns, much higher than expected. Device simulations have shown that further improving grain interior carrier lifetime would not give any improvement in device performance if grain boundary recombination cannot be reduced. This may explain why various extrinsic doping/alloying strategies that are anticipated to improve bulk qualities can improve device performance when the baseline efficiency is low (probably because grain interior lifetime is too low) but hardly further improve the efficiency if baseline efficiency is at a level of 12–13%. Therefore, strategies for effective grain boundary passivation are urgently needed. On the other hand, as long as the density of acceptor-like interface defects can be kept low, higher net carrier density will not lead to significant interfacial recombination[51]. Considering the radiatively limited lifetime versus carrier density of CZTSe materials (Supplementary Fig. 29), an increase in carrier density to about $5.0\times10^{16}\,cm^{-3}$ would be beneficial for the V_{OC} and efficiency when the intragrain lifetime can be increased to 100 ns, which is an essential direction to improve the efficiency towards 20% and beyond.

For sulfide Cu_2ZnSnS_4 (CZTS) solar cells, the microscopic carrier loss mechanisms can be investigated using the same framework, though some optoelectronic characterization such as EBIC and CL mapping could be more challenging. It is worth noting that the dominant loss mechanisms in CZTS may be different from that of CZTSe. The carrier density in CZTS is usually high ($>10^{16}\,cm^{-3}$), which, however, may impose more interfacial recombination even if the conduction band alignment is optimized[51]. Another important issue for CZTS is the significant PL red shift due to the dominating free-to-bound transition[52]. The impact of these loss mechanisms on the device performance needs to be carefully estimated and compared with non-radiative recombination losses at grain boundaries and grain interiors.

Conclusion

We have successfully unveiled most of the important microscopic loss mechanisms in our ≥12% efficiency CZTSe solar cells. The results indicate that the junction interface is well passivated by an epitaxial ZnSe nanolayer, the radiative recombination loss through bandgap fluctuation and/or electrostatic potential fluctuation is small and that the intragrain minority carrier lifetime is between 10 ns and 30 ns, all of which are encouraging characteristics for high efficiency solar cells. Instead, the high effective recombination velocity at grain boundaries ($\geq10^4\,cm\,s^{-1}$) and the relatively low net carrier density ($\sim2\times10^{15}\,cm^{-3}$) are the current main limiting factors of our CZTSe solar cells. This provides clear direction for improving the performance of Se-based kesterite solar cells. We believe the established framework to reveal the important microscopic loss mechanisms of thin-film solar cells could also be applicable to other emerging materials such as perovskite and antimony chalcogenides.

Methods

Cu–Zn–Sn metal precursor. CZTSe films were fabricated with sputtering stacked Cu–Zn–Sn metallic precursors on Mo-coated glass substrates, followed by a selenization growth process. The target composition of the CZTSe absorber is Cu/(Zn + Sn) ≈ 0.75 and Zn/Sn ≈ 1.1, measured with X-ray fluorescence spectrometer (ARL Perform'X 4200, Thermo Fisher Scientific, with Uniquant analysis software). The Cu, Zn and Sn targets have 99.999% purity. The precursor stacking order was Mo/Sn/Cu/Zn/Sn/Cu, and the sputtering pressure was about 0.2 Pa.

CZTSe selenization process. The metallic precursors were pre-alloyed at 250 °C for 15 min, followed by a soft selenization at 250–280 °C for 15 min in controlled low Se partial pressure. Then the substrates were ramped to 550 °C in 15 min and stayed at 550 °C for 8–10 min. The details of the annealing profile are described elsewhere[25]. All these annealing processes were performed in a custom-made furnace that can have independent temperature control of Se source, substrates and Se cracking barrel (schematic diagram in Supplementary Fig. 30). The controlling Se atmosphere by adjusting the Se source temperature and Se cracking barrel temperature was detailed in our early publication[53]. Some key points for the selenization processes are summarized as follows: (1) before selenization start, a pre-alloying treatment with temperature higher than 250 °C is important to fabricate compact films and also important to control the Sn loss and the thickness of $MoSe_2$ layer[54]; (2) a sufficient soft selenization with temperature below 300 °C (to prevent Sn loss) is important to control the bulk defects by turning Sn to Sn^{4+} and facilitating Zn diffusing to the top region before the synthesis of the CZTSe phase start at 350–400 °C (ref. [25]). This Zn diffusion process enabled by the soft selenization may be a key step for the formation of the epitaxial ZnSe nanolayer. The formation of a near-continuous ZnSe nanolayer may also require a slightly high Zn/Sn ratio (close to 1:1). For example, the ZnSe layer cannot be observed in the sample with Zn/Sn ratio lower than 1.05 (Supplementary Fig. 31). In this soft selenization, it is very important to use a reactive micro-molecule Se vapour (Se_2) under low Se partial pressure. High Se partial pressure will lead to poor Se diffusion[55]. (3) Sufficient Se partial pressure during high temperature annealing is important for grain growth.

CZTSe device fabrication. The CZTSe devices were fabricated with an architecture of Mo/CZTSe/CdS/i-ZnO/ZnO:Al/Ni/Al/MgF_2. A 20–50 nm CdS buffer layer was deposited at 85 °C using the chemical bath deposition method. A 50 nm i-ZnO layer and a 400–450 nm ZnO:Al layer were subsequently deposited using radio frequency and direct current sputtering, respectively, with an Ar working pressure of 0.2 Pa. The Ni/Al grids and 110 nm MgF_2 anti-reflector coating were deposited using electron beam evaporation. The total area of each device is about 0.24 cm^2 defined by mechanical scribing. Total area efficiencies are reported.

SEM, STEM and EDS. Morphological analysis was performed using a SEM (FEI Apreo LoVac). The TEM-ready samples were prepared using the in situ FIB lift-out technique on an FEI Dual Beam FIB/SEM. The samples were capped with sputtered C and e-Pt/I-Pt before milling. The transmittance electron microscopy (TEM) lamella thickness was ~100 nm. The samples were imaged on a Hitachi HD2700 STEM with high-resolution TEM mode and a JEOL JEM-F200. EDS spectra were acquired on Oxford INCA, Bruker Quantax EDS system.

***J–V* and EQE measurement.** The *J–V* curves were performed using a solar simulator (ABET IV Tester) with AM 1.5 G illumination (100 $mW\,cm^{-2}$) at room temperature in open air. The light intensity was calibrated with a Fraunhofer World PV Scale (WPVS) reference cell (KG3 filter). The scan was from −0.1 V to 0.5 V with a step of 4 mV and a dwell time of 2 ms. The temperature-dependent *J–V* data were measured using a vacuumed cryostat with quartz windows. The light intensity was adjusted according to the J_{SC} measured at standard condition (AM 1.5 G without cryostat). EQE data were acquired by measuring the short-circuit current with spectrally resolved monochromatic beam and locked-in amplifier, using calibrated Si and Ge photodiodes as references.

SIMS and ultraviolet photoelectron spectroscopy. The element depth profiles were recorded by SIMS (IMS-6F, CAMECA). A primary Cs^+ beam was used for 500 μm × 500 μm sampling area. Ultraviolet photoelectron spectroscopy was performed on Thermo Fisher ESCALAB 250Xi. A He I light source (21.2 eV) was used as excitation source. The spot size is 500 μm. The spectrometer was calibrated using Au $4f_7$ = 83.96 eV, Ag $3d_5$ = 368.21 eV and Cu $2p_3$ = 932.62 eV. The data was recorded at 0 V sample bias without etching process.

Raman mapping and Raman spectrum. Raman spectroscopy mapping was performed using a Renishaw inVia Raman microscope fitted with a 441 nm He–Cd laser as the excitation source, 1,800 l mm^{-1} grating and measured using a 100× objective. The focal point was above the surface of the sample to collect more signals from the surface. The pixel size was 2 μm × 2 μm. Raman spectrum on $MoSe_2$ back contact was performed using a 514 nm laser as the excitation, 1,800 l mm^{-1} grating and measured using a 100× objective. The focal point was on the surface of the sample.

EBIC. The EBIC measurements were performed on the cross-section of the finished device using an SEM (Zeiss ΣIGMA) extended with a tunable current amplifier. The devices were connected to a circuit that provided tunable bias. The EBIC images were obtained with a splitting mode, which was combined with SEM images of the same scanned region. The electron beam energy was 5 keV.

Cross-section KPFM and AFM. The cross-sectional KPFM measurements were conducted on a fresh cleaved CZTSe cell using atomic force microscopy (Bruker Dimension ICON SPM) with a scan rate of 0.200 Hz in a scan size of 8.5 μm (W) × 4.25 m (H). A brand new PtSi probe (Bruker SCM-PTSI) was used in these measurements, and the samples were measured using a two-pass scan (one for topography in contact mode and another for CPD maps in non-contact mode). The system deviation of CPD is about ± 10 mV. Surface AFM measurement was performed on an as-grown CZTSe sample using the same scan rate. In cross-section KPFM measurements, to prevent probe damage, we start the rough topology scan from the glass region, which is far from the cliff region of the cross-section, and gradually approach the glass/Mo interface. The glass/Mo interface can be identified by the sudden change of surface roughness because the cleaved glass is much smoother than the cross-section of Mo and CZTSe films.

When reaching the Mo and CZTSe interface, we slow the approach rate and then scan at the same rate until reaching the CZTSe/window layer. Once part of the window layer appears in the projected area, we stop approaching and focus on a relatively flat region for high-resolution KPFM measurements.

PL and TRPL. PL and TRPL were measured using a microscope customized for micro-PL measurements. The excitation source was a 532 nm pump from an EKSPLA PT210 laser at 1 MHz repetition rate and 10 ps pulse width. The TRPL signal was detected using a fibre-coupled InGaAs avalanche photodiode (ID210) and processed using the time-correlated single photon counting board (TimeHarp 260). The time binning is 25 ps.

CL mapping. A cross-section sample was prepared for CL by a plasma FIB (Thermo Fisher Helios G4 PFIB) with an in situ lift-out platform. The electron excitation profile was simulated by the Monte Carlo method using the CASINO software[55] (Supplementary Fig. 14) to determine the suitable thickness of the sample and acceleration voltage used in the CL measurement. On the basis of the simulation and considering that the average grain size is around 1 µm, 10 kV and 1 µm were used for the voltage and targeting thickness of the FIB milled sample, respectively. The sample was transferred and mounted on an in situ TEM grid with Pt welding after rough milling to about 2 µm thick. The sample was further polished using low beam current (0.3 nA) after lift out to achieve ~1 µm thickness. Before CL measurement, the sample received a final ion beam polish on both faces (Fischione NanoMill 1040) at low voltage (500 V) to ensure a clean and fresh surface for analysis. Analysis was conducted using a Delmic SPARC spectral cathodoluminescence system coupled to an FEI Nova Nano SEM 450 field-emission SEM.

3D device simulation. A commercial software package, Sentaurus technology computer-aided design was used to numerically examine the device physics. In this study, a 3D unit cell shown in Supplementary Fig. 24a was established in the simulator. In this unit cell, the absorber consists of five grains, one is larger (1.1 µm) and the other four are smaller with the same size (0.5 µm). The sizes of these grains were averaged from the TEM and SEM results (Supplementary Figs. 22 and 23). After all constitutional regions were generated in the simulator, the whole structure went through a meshing process to break down into millions of small elements, that is, cuboids. A smaller element allows for a higher accuracy to compute the spatial distribution of key fields such as carrier concentration. Meanwhile, it demands more computer resources as well. Hence the element size was refined only where the field variation is significant to balance between speed and accuracy. Afterwards, photogeneration was computed with the simple optical beam absorption method using the Beer–Lambert law. The complex refractive index of each layer was obtained from in-house characterization. The key semiconductor material parameters for electron simulation are listed in Supplementary Table 1 and obtained from either in-house characterization or the literature[56–58]. The ambient temperature in simulation is also 298.15 K to match the standard test condition. The carrier lifetime and mobility values are tuned to fit the experimental baseline.

After initialising all important fields and model parameters, the thermal equilibrium condition was first computed by solving five semiconductor equations, that is, the Poisson, drift-diffusion and carrier continuity equations, numerically. A well-established mesh and suitable solver help reach self-consistency fast. Subsequently, the impact of carrier generation and bias voltage was investigated by ramping these parameters dynamically. For each ramping step, the steady state was computed so that key fields can be extracted for further analysis. If necessary, a snapshot at a ramping step can also be saved to preserve spatial distribution of fields. Following this practice, the champion cell was reproduced by matching key performance characteristics. Afterwards, the impact of grain lifetime, carrier density, grain size and grain boundary recombination on cell performance was predicted, providing a guideline for future cell improvement.

Reporting summary. Further information on research design is available in the Nature Research Reporting Summary linked to this article.

Data availability

The datasets analysed and generated during the current study are included in the paper and its Supplementary Information. Source data are provided with this paper.

Code availability

The codes used for simulation within this paper are available from the corresponding author upon reasonable request.

Received: 18 January 2022; Accepted: 13 June 2022;
Published online: 21 July 2022

References

1. Creutzig, F. et al. The underestimated potential of solar energy to mitigate climate change. *Nat. Energy* **2**, 1–9 (2017).
2. Green, M. A. Third Generation Photovoltaics, *Springer* (2006).
3. Liu, F. et al. Emerging inorganic compound thin film photovoltaic materials: progress, challenges and strategies. *Mater. Today* **41**, 120–142 (2020).
4. Zakutayev, A. et al. Emerging inorganic solar cell efficiency tables (version 2). *J. Phys. Energy* **3**, 032003 (2021).
5. Osbel Almora, D. B. et al. Device performance of emerging photovoltaic materials (version 2). *Adv. Energy Mater.* **11**, 2102526 (2021).
6. Giraldo, S. et al. Progress and perspectives of thin film kesterite photovoltaic technology: a critical review. *Adv. Mater.* **31**, e1806692 (2019).
7. Walsh, A., Chen, S., Wei, S.-H. & Gong, X.-G. Kesterite thin-film solar cells: advances in materials modelling of Cu_2ZnSnS_4. *Adv. Energy Mater.* **2**, 400–409 (2012).
8. Son, D. H. et al. Effect of solid-H_2S gas reactions on CZTSSe thin film growth and photovoltaic properties of a 12.62% efficiency device. *J. Mater. Chem.* **7**, 25279–25289 (2019).
9. Wang, W. et al. Device characteristics of CZTSSe thin-film solar cells with 12.6% efficiency. *Adv. Energy Mater.* **4**, 1301465 (2014).
10. Best research-cell efficiency chart. NREL https://www.nrel.gov/pv/cell-efficiency.html (2022).
11. Siebentritt, S., Igalson, M., Persson, C. & Lany, S. The electronic structure of chalcopyrites-bands, point defects and grain boundaries. *Prog. Photovolt. Res. Appl.* **18**, 390–410 (2010).
12. Green, M. A. et al. Solar cell efficiency tables (version 59). *Prog. Photovolt. Res. Appl.* **30**, 3–12 (2021).
13. Yun, J. S. et al. Benefit of grain boundaries in organic–inorganic halide planar perovskite solar cells. *J. Phys. Chem. Lett.* **6**, 875–80 (2015).
14. Li, C. et al. Grain-boundary-enhanced carrier collection in CdTe solar cells. *Phys. Rev. Lett.* **112**, 156103 (2014).
15. Lin, T.-Y. et al. Alkali-induced grain boundary reconstruction on Cu(In,Ga)Se_2 thin film solar cells using cesium fluoride post deposition treatment. *Nano Energy* **68**, 104299 (2020).
16. Chen, S., Walsh, A., Gong, X. G. & Wei, S. H. Classification of lattice defects in the kesterite Cu_2ZnSnS_4 and $Cu_2ZnSnSe_4$ earth-abundant solar cell absorbers. *Adv. Mater.* **25**, 1522–39 (2013).
17. Martinho, F. et al. Persistent double-layer formation in kesterite solar cells: a critical review. *ACS Appl. Mater. Interfaces* **12**, 39405–39424 (2020).
18. Li, J., Wang, D., Li, X., Zeng, Y. & Zhang, Y. Cation substitution in earth-abundant kesterite photovoltaic materials. *Adv. Sci.* **5**, 1700744 (2018).
19. Romanyuk, Y. E. et al. Doping and alloying of kesterites. *J. Phys. Energy* **1**, 044004 (2019).
20. He, M., Sun, K., Suryawanshi, M. P., Li, J. & Hao, X. Interface engineering of p–n heterojunction for kesterite photovoltaics: a progress review. *J. Energy Chem.* **60**, 1–8 (2021).
21. Fonoll-Rubio, R. et al. Insights into interface and bulk defects in a high efficiency kesterite-based device. *Energy Environ. Sci.* **14**, 507–523. (2021).
22. Vishwakarma, M. et al. A direct measurement of higher photovoltage at grain boundaries in CdS/CZTSe solar cells using KPFM technique. *Sol. Energy Mater. Sol. Cells* **183**, 34–40 (2018).
23. Krause, M. et al. Microscopic origins of performance losses in highly efficient Cu(In,Ga)Se_2 thin-film solar cells. *Nat. Commun.* **11**, 4189 (2020).
24. Zhao, Y. et al. Monocrystalline CdTe solar cells with open-circuit voltage over 1 V and efficiency of 17%. *Nat. Energy* **1**, 1–7 (2016).
25. Li, J. et al. Defect control for 12.5% efficiency $Cu_2ZnSnSe_4$ kesterite thin-film solar cells by engineering of local chemical environment. *Adv. Mater.* **32**, 2005268 (2020).
26. Lee, Y. S. et al. $Cu_2ZnSnSe_4$ thin-film solar cells by thermal co-evaporation with 11.6% efficiency and improved minority carrier diffusion length. *Adv. Energy Mater.* **5**, 1401372 (2015).
27. Li, J. et al. Tailoring the defects and carrier density for beyond 10% efficient CZTSe thin film solar cells. *Sol. Energy Mater. Sol. Cells* **159**, 447–455 (2017).
28. Timo Wätjen, J., Engman, J., Edoff, M. & Platzer-Björkman, C. Direct evidence of current blocking by ZnSe in $Cu_2ZnSnSe_4$ solar cells. *Appl. Phys. Lett.* **100**, 173510 (2012).
29. Mendis, B. G. Fully depleted emitter layers: a novel method to improve band alignment in thin-film solar cells. *Semicond. Sci. Technol.* **34**, 055008 (2019).
30. Hages, C. J., Carter, N. J., Agrawal, R. & Unold, T. Generalized current-voltage analysis and efficiency limitations in non-ideal solar cells: case of $Cu_2ZnSn(S_xSe_{1-x})_4$ and $Cu_2Zn(Sn_yGe_{1-y})(S_xSe_{1-x})_4$. *J. Appl. Phys.* **115**, 234504 (2014).
31. Rau, U. Tunneling-enhanced recombination in Cu(In,Ga)Se_2 heterojunction solar cells. *Appl. Phys. Lett.* **74**, 112–114 (1999).
32. Hegedus, S. S. & Shafarman, W. N. Thin-film solar cells: device measurements and analysis. *Prog. Photovolt. Res. Appl.* **12**, 155–176 (2004).
33. Wang, K. et al. Thermally evaporated Cu_2ZnSnS_4 solar cells. *Appl. Phys. Lett.* **97**, 143508 (2010).
34. Barkhouse, D. A. R., Gunawan, O., Gokmen, T., Todorov, T. K. & Mitzi, D. B. Device characteristics of a 10.1% hydrazine-processed $Cu_2ZnSn(Se,S)_4$ solar cell. *Prog. Photovolt. Res. Appl.* **20**, 6–11 (2012).
35. Schwarz, T. et al. Atom probe tomography study of internal interfaces in $Cu_2ZnSnSe_4$ thin-films. *J. Appl. Phys.* **118**, 095302 (2015).

36. Cojocaru-Mirédin, O., Schwarz, T. & Abou-Ras, D. Assessment of elemental distributions at line and planar defects in Cu(In,Ga)Se_2 thin films by atom probe tomography. *Scr. Mater.* **148**, 106–114 (2018).
37. Gokmen, T., Gunawan, O., Todorov, T. K. & Mitzi, D. B. Band tailing and efficiency limitation in kesterite solar cells. *Appl. Phys. Lett.* **103**, 103506 (2013).
38. Rey, G. et al. On the origin of band-tails in kesterite. *Sol. Energy Mater. Sol. Cells* **179**, 142–151 (2018).
39. Shklovskii, B. I. & Efros, A. L. *Electronic Properties of Doped Semiconductors* vol. 45 (Springer, 2013).
40. Rau, U. & Werner, J. H. Radiative efficiency limits of solar cells with lateral band-gap fluctuations. *Appl. Phys. Lett.* **84**, 3735–3737 (2004).
41. Nichterwitz, M., Caballero, R., Kaufmann, C. A., Schock, H.-W. & Unold, T. Generation-dependent charge carrier transport in Cu(In,Ga)Se_2/CdS/ZnO thin-film solar-cells. *J. Appl. Phys.* **113**, 044515 (2013).
42. Heath, J. T., Cohen, J. D. & Shafarman, W. N. Bulk and metastable defects in $CuIn_{1-x}Ga_xSe_2$ thin films using drive-level capacitance profiling. *J. Appl. Phys.* **95**, 1000–1010 (2004).
43. Mendis, B. G., Bowen, L. & Jiang, Q. Z. A contactless method for measuring the recombination velocity of an individual grain boundary in thin-film photovoltaics. *Appl. Phys. Lett.* **97**, 092112 (2010).
44. Gershon, T. et al. The role of sodium as a surfactant and suppressor of non-radiative recombination at internal surfaces in Cu_2ZnSnS_4. *Adv. Energy Mater.* **5**, 1400849 (2015).
45. Tampo, H., Kim, K. M., Kim, S., Shibata, H. & Niki, S. Improvement of minority carrier lifetime and conversion efficiency by Na incorporation in $Cu_2ZnSnSe_4$ solar cells. *J. Appl. Phys.* **122**, 023106 (2017).
46. Hages, C. J. et al. Identifying the real minority carrier lifetime in nonideal semiconductors: a case study of kesterite materials. *Adv. Energy Mater.* **7**, 1700167 (2017).
47. Hempel, H., Hages, C. J., Eichberger, R., Repins, I. & Unold, T. Minority and majority charge carrier mobility in $Cu_2ZnSnSe_4$ revealed by Terahertz Spectroscopy. *Sci. Rep.* **8**, 14476 (2018).
48. Metzger, W. K. et al. Exceeding 20% efficiency with in situ group V doping in polycrystalline CdTe solar cells. *Nat. Energy* **4**, 837–845 (2019).
49. Kim, J. et al. High efficiency $Cu_2ZnSn(S,Se)_4$ solar cells by applying a double In_2S_3/CdS emitter. *Adv. Mater.* **26**, 7427–31 (2014).
50. He, M. et al. High efficiency $Cu_2ZnSn(S,Se)_4$ solar cells with shallow LiZn acceptor defects enabled by solution-based Li post-deposition treatment. *Adv. Energy Mater.* **11**, (2021).
51. Li, J. et al. Interface recombination of Cu_2ZnSnS_4 solar cells leveraged by high carrier density and interface defects. *Sol. RRL* **5**, 2100418 (2021).
52. Levcenko, S. et al. Deep defects in $Cu_2ZnSn(S,Se)_4$ solar cells with varying Se content. *Phys. Rev. Appl.* **5**, (2016).
53. Li, J. et al. Growth of $Cu_2ZnSnSe_4$ film under controllable Se vapor composition and impact of low Cu content on solar cell efficiency. *ACS Appl. Mater. Interfaces* **8**, 10283–92 (2016).
54. Li, J. et al. Barrier effect of the alloy layer during selenization: tailoring the thickness of $MoSe_2$ for efficient $Cu_2ZnSnSe_4$ Solar Cells. *Adv. Energy Mater.* **5**, 1402178 (2015).
55. Drouin, D. et al. CASINO V2. 42—a fast and easy-to-use modeling tool for scanning electron microscopy and microanalysis users. *Scanning* **29**, 92–101 (2007).
56. Pu, A. et al. Sentaurus modelling of 6.9% Cu_2ZnSnS_4 device based on comprehensive electrical & optical characterization. *Sol. Energy Mater. Sol. Cells* **160**, 372–381 (2017).
57. Jones, G. & Woods, J. The electrical properties of zinc selenide. *J. Phys. D* **9**, 799 (1976).
58. El Otmani, R., El Manouni, A., & Al Maggoussi, A. Numerical simulation of CZTSe based solar cells using different back surface field layers: improvement and comparison. *J. Electron. Mater.* **50**, 2021–2033 (2021).

Acknowledgements

J.L., J.H., X.H. and M.A.G. acknowledge the financial support of the Australian government through the Australian Renewable Energy Agency (ARENA) (grant number 2017/RND006), Baosteel (grant number LP150100911). X.H. acknowledges the financial support of the Australian Research Council (ARC) Future Fellowship (FT190100756). J.L. acknowledges the support from Australian Centre of Advanced Photovoltaics (ACAP, RG200768-A). T.U. acknowledges support by the European Union's Horizon 2020 research and innovation programme under grant agreement numbers 777968 (INFINITE-CELL project) and 952982 (Custom-Art project). Responsibility for the views, information or advice expressed herein is not accepted by the Australian government. We thank C. Jiang from the US National Renewable Energy Laboratory for the discussion of KPFM measurements. We thank C. Li for the reflectance measurements. We acknowledge the facilities and the scientific and technical assistance of Microscopy Australia at the Electron Microscope Unit (EMU), the Spectroscopy Laboratory and the Solid State and Elemental Analysis Unit within the Mark Wainwright Analytical Centre (MWAC) at UNSW Sydney.

Author contributions

J.L. and X.H. conceived the idea. X.H. and M.A.G. supervised the project. J.L. fabricated the CZTSe films and solar cells; conducted *J–V*, EQE, *J–V–T*, CV/DLCP, Raman mapping, SEM, EBIC measurements and most of the data analysis; and wrote the manuscript. J.H. analysed the HR-STEM, EBIC and CL data. F.M. developed the 3D device simulation model. F.M. and J.L. performed the 3D simulation. Y.Y., J.L. and H.S. conducted KPFM measurements. J.H. and J.C. fabricated the FIB sample for CL mapping and STEM-EDS measurements. K.P., J.H., R.D.T. and J.L. conducted the CL mapping. R.F.W., S.C., R.D.T. and J.H. conducted the STEM-EDS measurements. R.L.C., Z.H. and J.L. conducted the PL and TRPL measurements. X.Y. did the Raman measurements. M.H. and K.S. assisted in precursor and window layer fabrication. H.L. assisted in EBIC measurements. All authors discussed and commented on the manuscript.

Competing interests

The authors declare no competing interests.

Additional information

Supplementary information The online version contains supplementary material available at https://doi.org/10.1038/s41560-022-01078-7.

Correspondence and requests for materials should be addressed to Jianjun Li or Xiaojing Hao.

Peer review information *Nature Energy* thanks the anonymous reviewers for their contribution to the peer review of this work.

Reprints and permissions information is available at www.nature.com/reprints.

Publisher's note Springer Nature remains neutral with regard to jurisdictional claims in published maps and institutional affiliations.

Open Access This article is licensed under a Creative Commons Attribution 4.0 International License, which permits use, sharing, adaptation, distribution and reproduction in any medium or format, as long as you give appropriate credit to the original author(s) and the source, provide a link to the Creative Commons license, and indicate if changes were made. The images or other third party material in this article are included in the article's Creative Commons license, unless indicated otherwise in a credit line to the material. If material is not included in the article's Creative Commons license and your intended use is not permitted by statutory regulation or exceeds the permitted use, you will need to obtain permission directly from the copyright holder. To view a copy of this license, visit http://creativecommons.org/licenses/by/4.0/.

© The Author(s) 2022

nature research

Corresponding author(s): Jianjun Li, Xiaojing Hao

Solar Cells Reporting Summary

Nature Research wishes to improve the reproducibility of the work that we publish. This form is intended for publication with all accepted papers reporting the characterization of photovoltaic devices and provides structure for consistency and transparency in reporting. Some list items might not apply to an individual manuscript, but all fields must be completed for clarity.

For further information on Nature Research policies, including our data availability policy, see Authors & Referees.

Experimental design

Please check: are the following details reported in the manuscript?

1. Dimensions

Item	Reported	Details
Area of the tested solar cells	[X] Yes [ ] No	Methods - The total area of each device is about 0.24 cm2 defined by mechanical scribing. Total area efficiencies are reported.
Method used to determine the device area	[X] Yes [ ] No	Methods -The total area of each device is about 0.24 cm2 defined by mechanical scribing. Total area efficiencies are reported.

2. Current-voltage characterization

Item	Reported	Details
Current density-voltage (J-V) plots in both forward and backward direction	[ ] Yes [X] No	Hysteresis is not observed.
Voltage scan conditions *For instance: scan direction, speed, dwell times*	[X] Yes [ ] No	Methods -The scan was from -0.1V to 0.5V with a step of 4 mV and a dwell time of 2 ms.
Test environment *For instance: characterization temperature, in air or in glove box*	[X] Yes [ ] No	Methods - The cells were measured at room temperature in open air.
Protocol for preconditioning of the device before its characterization	[ ] Yes [X] No	No light soaking or other protocol for preconditioning was employed
Stability of the J-V characteristic *Verified with time evolution of the maximum power point or with the photocurrent at maximum power point; see ref. 7 for details.*	[X] Yes [ ] No	Supplementary Figure 1b.The J-V characteristics was tracked after storage aging for 42 days and 167 days.

3. Hysteresis or any other unusual behaviour

Item	Reported	Details
Description of the unusual behaviour observed during the characterization	[ ] Yes [X] No	No hysteresis and other unusual behavior has been observed by authors.
Related experimental data	[ ] Yes [X] No	No hysteresis and other unusual behavior has been observed by authors.

4. Efficiency

Item	Reported	Details
External quantum efficiency (EQE) or incident photons to current efficiency (IPCE)	[X] Yes [ ] No	Provided EQE in Figure 1b in main manuscript
A comparison between the integrated response under the standard reference spectrum and the response measure under the simulator	[X] Yes [ ] No	See the integrated Jsc from EQE in Figure 1b in main manuscript. The integrated Jsc is slightly (0.1mA/cm2) higher than the Jsc measured under simulator.
For tandem solar cells, the bias illumination and bias voltage used for each subcell	[ ] Yes [X] No	Not applicable

5. Calibration

Item	Reported	Details
Light source and reference cell or sensor used for the characterization	[X] Yes [ ] No	Methods - The J-V curves were performed using a solar simulator (ABET IV Tester) with AM1.5 G illumination (100 mW cm–2) at room temperature in open air. The light intensity was calibrated with a Fraunhofer WPVS reference cell (KG3 filter) reference cell.

Confirmation that the reference cell was calibrated and certified	☒ Yes ☐ No	Methods - The light intensity was calibrated with a Fraunhofer WPVS reference cell (KG3 filter) reference cell.
Calculation of spectral mismatch between the reference cell and the devices under test	☐ Yes ☒ No	Certificated silicon solar cells are commonly used as the reference solar cell for performance test of kesterite thin film solar cells. For kesterite CZTSe the band gap energy (Eg=1.0 eV to 1.05 eV) is close to silicon solar cell (Eg=1.10 eV).

6. Mask/aperture

Size of the mask/aperture used during testing	☐ Yes ☒ No	Not applicable as no mask/aperture is used.
Variation of the measured short-circuit current density with the mask/aperture area	☐ Yes ☒ No	Not applicable as no mask/aperture is used.

7. Performance certification

Identity of the independent certification laboratory that confirmed the photovoltaic performance	☐ Yes ☒ No	A sister cell with 12.5% efficiency has been independently confirmed by Fujian Metrology Institute/National PV Industry Measurement and Testing Center, NPVM. The device performance has been cross-checked by UNSW and Jinan University. The light intensity of our solar simulator for J-V and EQE measurement was calibrated by standard Silicon and Ge cells which were calibrated by Fraunhofer.
A copy of any certificate(s) *Provide in Supplementary Information*	☐ Yes ☒ No	The light intensity of our solar simulator for J-V and EQE measurement was calibrated by standard Silicon and Ge cells which were calibrated by Fraunhofer. We do not claim record efficiency in this work.

8. Statistics

Number of solar cells tested	☒ Yes ☐ No	Supplementary Figure 1a.
Statistical analysis of the device performance	☒ Yes ☐ No	Supplementary Figure 1a.

9. Long-term stability analysis

Type of analysis, bias conditions and environmental conditions *For instance: illumination type, temperature, atmosphere humidity, encapsulation method, preconditioning temperature*	☒ Yes ☐ No	Supplementary Figure 1b.The J-V characteristics was tracked after storage aging for 42 days and 167 days. Long term stability testing is beyond the scope of this article.